



Activating earth-abundant insulator BaSO₄ for visible-light induced degradation of tetracycline

Qiaoshan Chen^a, Hanqiang Zhou^a, Jianchun Wang^a, Jinhong Bi^{a,*}, Fan Dong^{b,*}

^a Department of Environmental Science and Engineering, Fuzhou University, Minhou, Fujian 350108, China

^b Yangtze Delta Region Institute (Huzhou) & Institute of Fundamental and Frontier Sciences, University of Electronic Science and Technology of China, Huzhou 313000, China

ARTICLE INFO

Keywords:

Visible-light photocatalysis
BaSO₄
Tetracycline
Heterostructure
Degradation mechanism

ABSTRACT

Vast progress in semiconductor photocatalysis has been witnessed, while the earth-abundant insulators were seldomly explored. In this work, we exploited insulator BaSO₄ as photocatalyst by constructing a novel branch of insulator-semiconductor heterostructure with the narrow-gap CuS. The finely designed BaSO₄-CuS heterostructure achieved a tetracycline (TC) degradation pseudo-first-order kinetic constant of $1.4 \times 10^{-2} \text{ min}^{-1}$, which was 311, 21 and 18 times higher than that of BaSO₄, CuS and their physical mixture, respectively. Density functional theory (DFT) calculations unraveled that the intense Cu-O covalent interaction created a specific channel for interfacial electrons transfer from semiconductor to insulator. The elevated redox potential of CuS is vital for the accumulation of $\cdot\text{O}_2^-$ and motivation of $\cdot\text{OH}$, thus remarkably accelerating TC mineralization. Furthermore, the degradation pathway and intermediates of TC were thoroughly studied through LC-MS. The current work provides new perspectives to harvest visible-light-driven insulator photocatalysts and demonstrates its promising applications for environmental remediation.

1. Introduction

The antibiotics have been widespread used in recent decades and their unsuitable discharge in wastewater bodies poses great threat to aquatic wildlife and human health [1,2]. Tetracycline (TC), as a typical broad-spectrum antibiotic, possesses stable structure and poor biodegradability, and is difficult to be eliminated. The traditional non-destructive techniques for TC removal like adsorption, coagulation or membrane separation can only transfer the pollutants to another phase instead of decomposing it [3–5]. Meanwhile, the chemical or biological processes are limited by the complicated operation, expensive infrastructure and possible secondary pollution [6,7]. Noteworthily, visible-light photocatalytic technology has created a new avenue in pollutant degradation on account of the simple operation, low-cost and environmental friendliness [8,9]. Versatile semiconductor catalysts have been developed for pollutants photo-degradation such as TiO₂, ZnO, AgX (X = Cl, Br and I), metal-organic frameworks (MOFs) and covalent organic frameworks (COFs) [10–14].

Compared to relatively rare and costly semiconductors, the earth-abundant insulators hold various merits of economic advantage, ease of fabrication, robust chemical stability and especially stronger redox

capacity to serve as photocatalytic materials [15,16]. Moreover, the insulator materials are widely utilized in the scenes exposed to sunlight as ceramic, coating and building materials, benefitting for the adequate utilization of the solar energy. Hence, insulator photocatalysis has recently gained tremendous awareness and become an appealing research spot [17,18]. In succession, insulator BaCO₃, SrSO₄, SrCO₃ and CaSO₄ were developed as catalysts or co-catalysts and displayed superior photocatalytic activity in NO removal and methylene blue degradation [19–22]. The major bottleneck for insulator photocatalysts is the exceeding wide band gap for light excitation, while the wide gap could offer it excellent redox ability. The paradox also exists in semiconductor photocatalysis, where light absorption and redox ability could not be simultaneously obtained in a single material [23,24].

Constructing heterostructure, especially with narrow band gap semiconductor, has been documented to be an effective way to modify wide-gap semiconductor and solve the paradox [25,26]. For example, copper sulfide (CuS), as a highly-active narrow-gap semiconductor, has been applied to modify TiO₂, ZnO and ZnS for Cr (VI) reduction, methylene blue degradation and hydrogen production, respectively [27–30]. Accordingly, it is reasonable to assume that forming heterostructure between wide-gap insulator and narrow-gap semiconductor

* Corresponding author.

E-mail addresses: bijinhong@fzu.edu.cn (J. Bi), dfctbu@126.com, dongfan@uestc.edu.cn (F. Dong).

<https://doi.org/10.1016/j.apcatb.2022.121182>

Received 23 November 2021; Received in revised form 26 January 2022; Accepted 2 February 2022

Available online 4 February 2022

0926-3373/© 2022 Elsevier B.V. All rights reserved.

could synchronously achieve the excellent visible-light harvesting ability and desired redox capacity. In addition, the good template property of insulator is feasible to gain better dispersity, more exposed active sites and accelerated separation of photoinduced charges [31]. However, realizing the electrons transfer from semiconductor to the insulator and exploring the interfacial charge separation are still greatly challenging.

Herein, a proof-of-concept experiment was attempted in this work by constructing heterostructure between barium sulfate (BaSO_4 , n-type, 5.1 eV) and copper sulfide (CuS , p-type, 2.3 eV) for efficient tetracycline photodegradation under visible light. The BaSO_4 with refractive index of 1.64 can be penetrated with sunlight without loss, which is beneficial for the sufficient light utilization of the semiconductor [20]. The greatly elevated tetracycline degradation kinetics constant of the heterostructure demonstrated the incorporated insulator offered stronger redox capacity. The interaction between BaSO_4 and CuS , as well as the interfacial photoinduced charge transfer was thoroughly studied through density functional theory (DFT) calculations. Furthermore, electron spin resonance (ESR) and liquid chromatograph tandem mass spectrometer (LC-MS) were conducted to fully analyze the produced oxidative radicals, intermediates and degradation process of tetracycline. This work deepens the insights for reasonably designing and constructing earth-abundant insulator photocatalytic materials for aquatic organic pollutants purification.

2. Experimental

2.1. Chemicals

Copper nitrate trihydrate ($\text{Cu}(\text{NO}_3)_3 \cdot 3\text{H}_2\text{O}$), sodium thiosulfate ($\text{Na}_2\text{S}_2\text{O}_3 \cdot 5\text{H}_2\text{O}$), anhydrous sodium sulfate (Na_2SO_4), potassium ferri-cyanide ($\text{K}_3\text{Fe}(\text{CN})_6$), potassium ferrocyanide ($\text{K}_4\text{Fe}(\text{CN})_6 \cdot 3\text{H}_2\text{O}$) and potassium chloride (KCl) were purchased from Aladdin Reagent Co., Ltd. Barium sulfate (BaSO_4), 5,5-dimethyl-1-pyrroline N-oxide (DMPO) and 2,2,6,6-tetramethylpiperidine (TEMP) were purchased from Sino-pharm Chemical Reagent Co., Ltd. All the chemicals were used without further purification.

2.2. Synthesis of catalysts

The BaSO_4 - CuS heterostructure was prepared through an in-situ deposition-precipitation procedure under oil bath by using commercial BaSO_4 as the template. Typically, 0.3 g BaSO_4 was dispersed in 40 mL ethanol and treated with ultrasound for uniformly dispersion. Under vigorous stirring, 1.14 g $\text{Cu}(\text{NO}_3)_2 \cdot 3\text{H}_2\text{O}$ and 1.17 g $\text{Na}_2\text{S}_2\text{O}_3 \cdot 5\text{H}_2\text{O}$ were successively dissolved into the above suspension. The mixture was then reacted under oil bath at 70 °C for 4 h. After reaction, the solids were collected by centrifugation, washed with distilled water and ethanol for three times, and then dried at 60 °C for 12 h. The resulted sample was named BC3 and other mass ratio of BaSO_4 - CuS heterostructure were 2:2 (BC2) and 2:4 (BC4), respectively. In comparison, the pure CuS was prepared through the similar method without adding BaSO_4 .

2.3. Characterization

The X-ray diffraction (XRD) patterns of the samples were obtained at 2θ from 5° to 80° in Rigaku MiniFlex 600 X-ray diffractometer that employs $\text{Cu K}\alpha$ radiation ($\lambda = 1.5406 \text{ \AA}$) at 15 mA and 40 kV. To analyze surface chemical composition, X-ray photoelectron spectroscopy (XPS) was examined in X-ray photoelectron spectroscopy (PHI Quantum 2000) consisting of $\text{Al K}\alpha$ X-ray source, hemispherical analyzer and multi-axial adjustable sample stage. The crystalline morphology, structure and elemental mapping of the catalysts were observed through field emission scanning electron microscope (FESEM, Hitachi SU8000) and transmission electron microscope (TEM, JEOL model JEM 2010 EX). The specific Brunauer-Emmett-Teller (BET) surface areas were tested in Micrometrics ASAP 2020 at 77 K. UV-vis diffuse reflectance (UV-vis

DRS) was performed on UV-vis-NIR spectrophotometer (Varian Cary 500) to evaluate the optical characteristics of the catalysts at room temperature. The photoluminescence (PL) spectra were measured at 320 nm excited light by Edinburgh FL/FS900 spectrophotometer.

2.4. Theoretical calculation

The DFT calculations were conducted by employing the universal generalized gradient correlation function and Vienna ab initio simulation package (VASP5.4). A plane-wave basis set with a cutoff energy at 400 eV within the framework of the projector augmented wave method was adopted. The Gaussian smearing width was set to 0.2 eV. The Brillouin zone was sampled with a $3 \times 3 \times 1$ K points. All atoms were allowed to converge to 0.01 eV \AA^{-1} . The supercell of CuS and BaSO_4 was firstly released, respectively and then the heterostructure supercell was constructed by placing CuS supercell with 48 copper and sulfur atoms and on the plane of BaSO_4 supercell with 16 barium atoms, 16 sulfur atoms and 64 oxygen atoms.

2.5. Photoelectrochemical measurement

Electrochemical studies of photocatalysts were performed in the traditional cell with three electrodes, using Ag/AgCl and platinum plate as reference and counter electrode, respectively. The working electrode was produced as follows: photocatalyst (5 mg) was dispersed in N, N-dimethylformamide (0.5 mL) fully by ultrasound and the suspension (10 μL) was dropped to the fluoride-tin oxide glass substrate with cover area of 0.25 cm^2 , and dried at room temperature naturally. The uncovered areas were insulated by epoxy. The Mott-Schottky and electrochemical impedance spectroscopy (EIS) were tested with a ZAHNER IM6 electrochemical workstation in 0.2 M Na_2SO_4 solution and 10 mM $\text{K}_3[\text{Fe}(\text{CN})_6]/0.1 \text{ M}$ KCl mixed solution, respectively. The photocurrent data were recorded on electrochemical workstation (CHI650E, CH Instruments Inc., Shanghai) by using 0.2 M Na_2SO_4 and 300 W Xe lamp with a 420 nm filter as electrolyte and light source, respectively. Each electrochemical test was repeated for three times under ambient condition.

2.6. Tetracycline adsorption and photo-degradation

The adsorption experiments were carried out by adding 20 mg catalysts into 100 mL TC solution in concentration of 20 mg/L at 150 rpm and 25 °C under darkness to reach adsorption-desorption equilibrium. At interval time, 2 mL solution was sampled and filtered with a 0.22 μm millipore filter for concentration determine at 357 nm with UV-vis spectrophotometer (Cary 5000, Agilent). The adsorption capacity was calculated according to the equation: $q = (C_0 - C_t)V/m$, where C_0 and C_t was the TC concentration at 0 and t min, respectively, V was the volume of TC solution and m was mass of catalysts. The kinetic data was fitted by the widely used pseudo-first order and pseudo-second order models. The linear equations were listed as follows: $\ln(q_e - q_t) = \ln q_e - k_1 t$ and $t/q_t = 1/k_2 q_e^2 + t/q_e$, where q_t and q_e was adsorption capacity at time t and equilibrium time, respectively, k_1 and k_2 was pseudo-first order model rate constant and pseudo-second order model rate constant [32,33]. The influence of pH and catalyst dosage on the adsorption ability were probed by adjusting pH at 3, 5, 7, 9, 11 and catalyst dosage at 5, 10, 20 mg. The photocatalytic activity of the as-synthesized catalysts was evaluated by tetracycline degradation using 300 W Xenon lamp (PLS-SXE300C) with 420 nm filter as the light source. In a typical experiment, 20 mg photocatalyst was dispersed in 100 mL 20 mg/L TC solution. To accelerate the adsorption process, the suspension was treated with ultrasound for 30 min and then stirred for 30 min to reach adsorption equilibrium in darkness. After visible-light irradiation, 3 mL solution was separated and filtered at regular time intervals for further full-spectrum measurement with UV-vis spectrophotometer. The degradation efficiency was determined using the equation: $\eta (\%) = (C_0 -$

$C_t/C_0 \times 100$. To quantitatively examine the reaction kinetics, the pseudo-first order model was appointed to simulate the degradation data: $\ln(C_0/C_t) = kt$, where k is the pseudo-first order rate constant. The photocatalytic activity for ciprofloxacin (CIP) degradation was evaluated by dispersing 200 mg catalysts in 10 mg/L CIP and the concentration was determined at 277 nm by UV-vis spectrophotometer.

The removal rate of total organic carbon (TOC) was measured on a TOC analyzer (TOC-L CPH) and the mineralization yield was determined by the equation: $\text{mineralization yield (\%)} = (\text{TOC}_0 - \text{TOC}_t)/\text{TOC}_0 \times 100$, where TOC_0 and TOC_t was the TOC value at 0 and t min, respectively. The toxicity of TC and its intermediates during the reaction process was assessed using a bioluminescent assay with marine photobacteria, *Vibrio fischeri*, according to ISO 11348 (1994) in a toxicity analyzer (Glomax Multi, Promega Co., USA). The bacterial bioluminescent signals were measured after 15-min incubation at $20 \pm 1^\circ\text{C}$. The bioluminescence inhibition ratio was calculated by the following equation [34,35]:

$$\text{Bioluminescence inhibition ratio} = \frac{L_{\text{blank}} - L_{\text{sample}}}{L_{\text{blank}}} \times 100\%$$

L_{blank} and L_{sample} represented the bioluminescent signals after 15-min incubation in the treatment of deionized water and tested samples, respectively. All the testing and control experiments were performed in triplicate and higher bioluminescence inhibition ratio indicated higher toxicity of the samples. The stability of the as-synthesized catalysts was tested through cyclic experiments (2 h per cycle) for four cycles under the same reactive condition. The ESR spectra were recorded after light irradiation for 10 min by using DMPO to trap $\cdot\text{O}_2^-$, $\cdot\text{OH}$ and TEMP to trap $^1\text{O}_2$, on a EDX nano spectrometer at frequency of 100 kHz. The generation of H_2O_2 in the photocatalytic process was detected by the UV-vis spectrometer at a peak of 350 nm with otolidine as peroxide indicator.

The photodegradation intermediates of TC were analyzed by LC-MS (TSQ Quantum Access MAX). The TC and intermediates were separated on an eclipse plus C18 column (Agilent, 250 mm \times 4.6 mm, 5 μm) with mobile phase (0.8 mL/min) consisting of 0.1% formic acid solution and methyl alcohol. The liquid phase conditions were set as follows: The flow compatibility ratio was formic acid (0.1%):methanol = 65:35, the wavelength of the detector was 357 nm, and the injecting volume was 10 μL . The mass spectrometer was operated in positive ionization mode

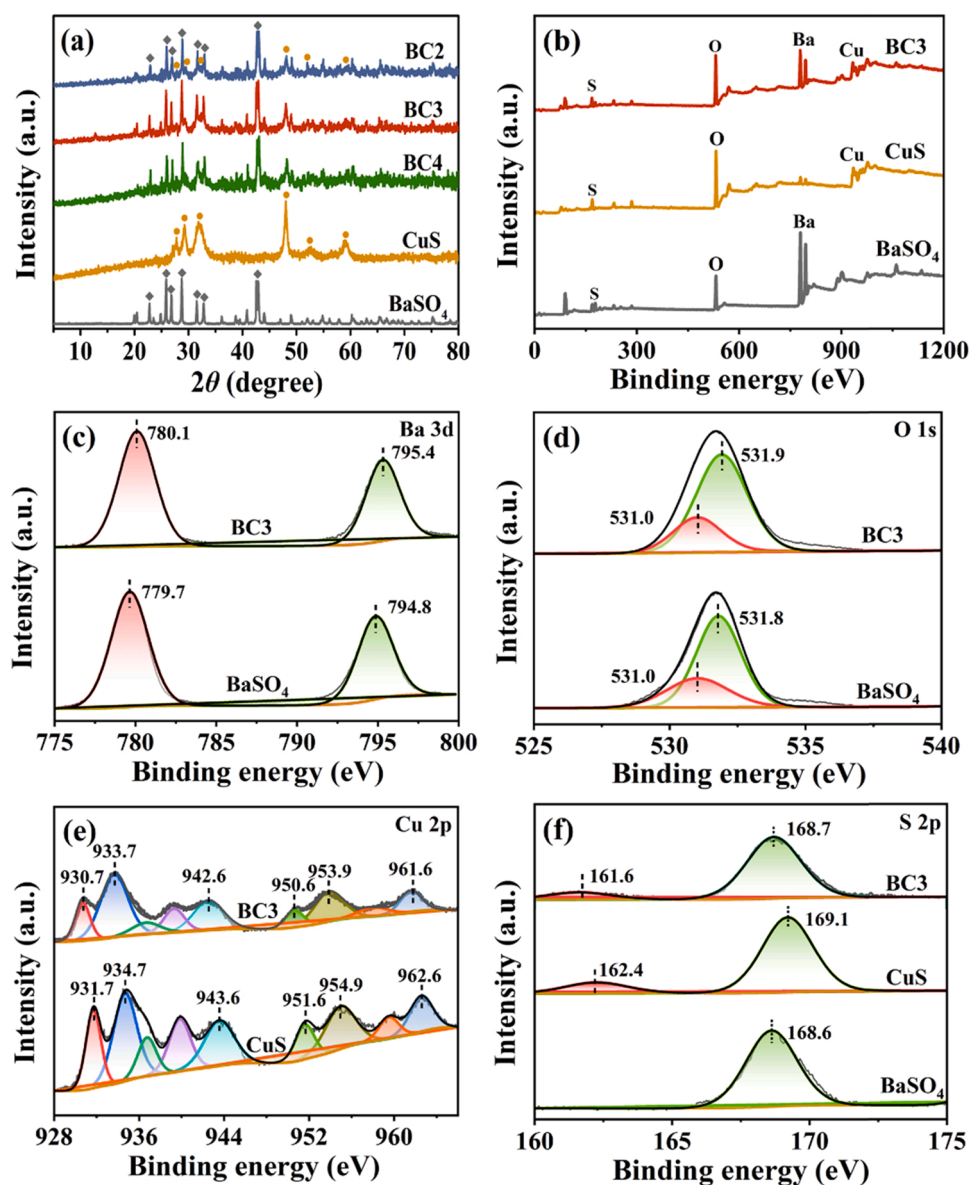


Fig. 1. XRD patterns of BaSO₄, CuS and BaSO₄-CuS series (a), full (b) and high-resolution XPS spectra of BaSO₄, CuS and BC3 for Ba 3d (c), O 1s (d), Cu 2p (e) and S 2p (f).

and the data was obtained in a scan range of 100–720 m/z . Nitrogen with purity > 99.9% and nitrogen with purity > 99.999% was used as carrier gas and impact gas, respectively. The inorganic ions formed during the TC degradation including NH_4^+ , NO_2^- and NO_3^- were quantified with an ion chromatograph (ICS-1100, Dionex, Thermo Scientific).

3. Results and discussion

3.1. Chemical composition and microstructure

As evidenced by the XRD patterns in Fig. 1a, the BaSO_4 -CuS heterostructure was successfully constructed. The heterostructure sample of BC2, BC3 and BC4 all exhibited the typical peaks at 2θ of 22.8° , 25.8° , 26.8° , 28.7° , 31.5° , 32.8° and 42.6° , respectively corresponding to lattice plane (110), (021), (210), (121), (211), (002) and (140) of orthorhombic BaSO_4 (JCPDS: 24-1035) [36]. Simultaneously, the characteristic diffraction peaks of hexagonal CuS (JCPDS: 06-0464) were also detected in the heterostructure samples at 2θ of 27.7° , 29.3° , 31.8° , 47.9° , 52.7° and 59.3° , indexing to lattice planes of (101), (102), (103), (110), (108) and (116), respectively [37]. Especially, the intensity of the representative CuS peak at 47.9° in the heterostructures was strengthened with the increase of CuS loading amount. Additionally, no obvious impurity peaks were detected, implying pure heterostructure photocatalysts were obtained.

The XPS was further introduced to characterize the surface chemical states of the catalysts and the full range spectrum of BC3 clearly showed the existence of Cu, Ba, O and S elements (Fig. 1b). The Ba 3d spectrum of pure BaSO_4 presented two main peaks at 779.7 and 794.8 eV corresponding to Ba 3d_{5/2} and Ba 3d_{3/2} respectively [16], while the peaks in BC3 shifted to higher bonding energies at 780.1 and 795.4 eV after interacting with CuS (Fig. 1c). For O 1s high-resolution spectrum of BaSO_4 , the characteristic peaks at 531.0 and 531.8 eV are ascribed to hydroxy and sulfate, respectively (Fig. 1d). In Fig. 1e, the two deconvoluted peaks of CuS appearing at bonding energies of 931.7 and 951.6 eV were assigned to Cu 2p_{3/2} and Cu 2p_{1/2}, which shifted towards the lower direction to 930.7 and 950.6 eV when forming heterostructure [38]. A set of doublets located at 934.7 and 954.9 eV accompanied by two separate set-up satellites at 943.6 and 962.6 eV is indicative of the presence of Cu^{2+} in CuS [39,40]. The high-resolution S 2p spectrum of

BC3 exhibited two deconvoluted peaks at 161.6 and 168.7 eV (Fig. 1f), relating to S^{2-} species in CuS and oxidized sulfur species (SO_4^{2-}) in BaSO_4 [41]. Conspicuously, the photoelectron peaks for Ba, O and S in BaSO_4 all shifted to higher bonding energies after formation of heterostructure along with the shifting of Cu and S peaks in CuS to lower direction, revealing the strong interaction and electron transfer between BaSO_4 and CuS [42].

The pure BaSO_4 presented in form of rod or block with smooth surface in size of 300–800 nm (Fig. 2a), while the synthesized pure CuS were severely aggregated nanoparticles without external shape (Fig. 2b). When growing on the surface of BaSO_4 , the morphology of CuS dramatically changed from irregular grains to nanosheets, which could be attributed to the transform of crystalline nucleation pathway from homogenous nucleation to heterogeneous nucleation [43,44]. As depicted in Fig. 2c, the CuS nanosheets tightly stucked to the BaSO_4 surfaces, verifying the successful construction of the heterostructure. The low-magnification FESEM image in Fig. 2d demonstrated that CuS nanosheets were sufficiently and uniformly decorated on BaSO_4 .

The core-shell hybrid structure was further observed through TEM, where BaSO_4 maintained its block shape and CuS nanosheets coated outside as the shell layer (Fig. 3a). The EDX analysis confirmed the uniform distribution of Ba, O, Cu and S elements on the BC3 heterostructure (Fig. 3d). The HRTEM images of the selected areas exhibited lattice fringes of 0.33 and 0.28 nm, matching well with the (210) plane of BaSO_4 and the (103) plane of CuS, respectively [45]. The clearly observed border between BaSO_4 and CuS illustrated the formation of intimate interface, which was an essential prerequisite for their interaction and was beneficial for the charge transfer (Fig. 3b and c). The N_2 adsorption-desorption isotherms of BaSO_4 , CuS and BC3 sample all presented in type IV with H3 hysteresis loops measured at 77 K in P/P_0 range of 0.8–1.0, resulting from the tidy arrangement of catalysts and capillary condensation of the mesoporous structure (Fig. S1) [46]. The specific surface area of BaSO_4 , CuS and BC3 was estimated to be 3.44, 9.19 and 11.43 m^2/g , respectively (Table S1). The BJH pore size distribution study revealed CuS and BC3 had similar mesoporous structure. The slightly increased surface area of BC3 was possibly advantageous for pollutants adsorption and the photocatalytic reaction.

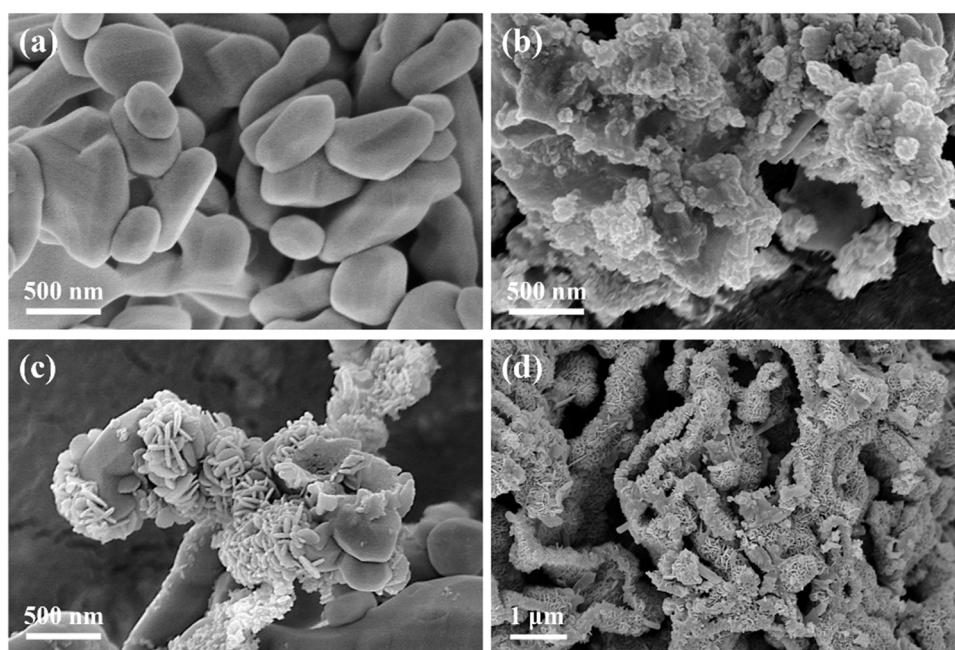


Fig. 2. FESEM images of BaSO_4 (a), CuS (b) and BC3 at high magnification (c) and low magnification (d).

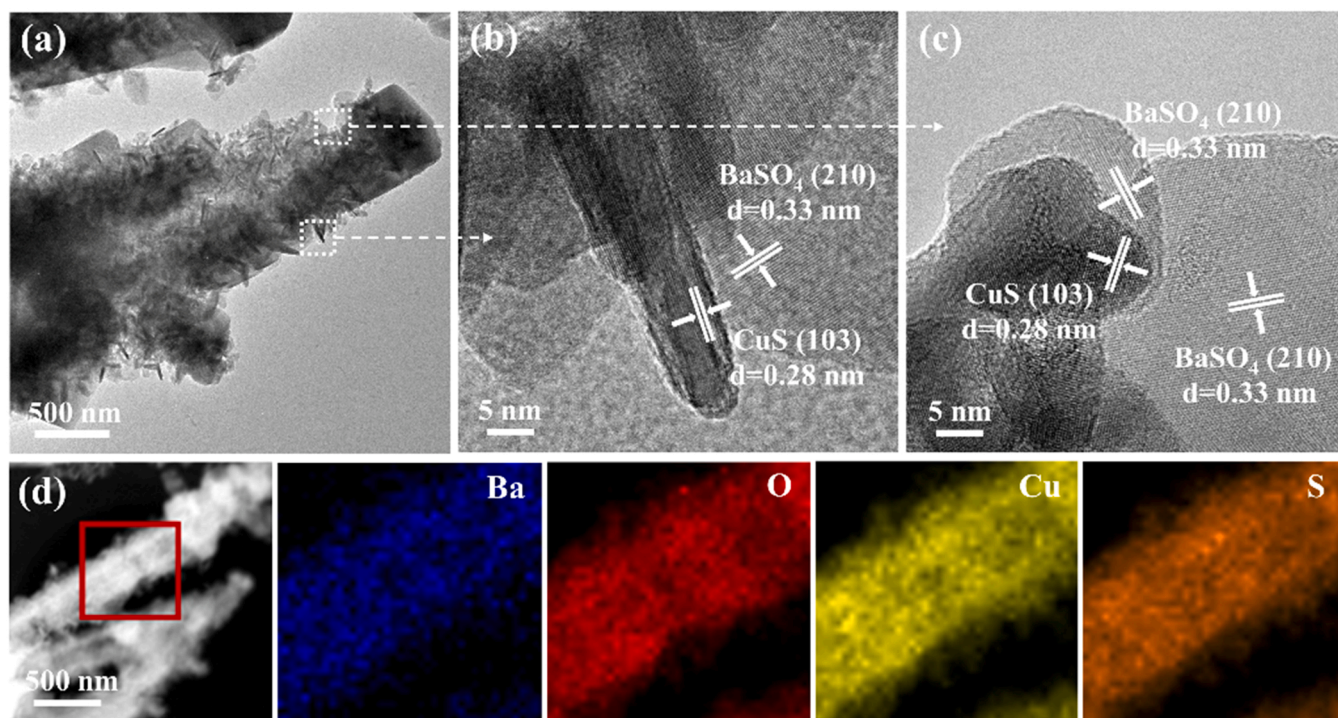


Fig. 3. TEM image (a), HRTEM images (b and c) and EDX elemental mapping of Ba, O, Cu and S (d) over BC3.

3.2. Photoelectrochemical properties

The optical properties of as-prepared products were firstly analyzed by UV-vis DRS. As estimated, BaSO₄ showed minimal incited-light absorption and the absorption edge appeared approximately at 240 nm (Fig. 4a). The corresponding band gap of BaSO₄ was calculated to be

5.14 eV according to the intercept of tangents to the plots of $(\alpha h\nu)^{1/2}$ versus photon energy (Fig. 4b). Noticeably, as the incorporation of narrow-gap semiconductor CuS (2.33 eV), an obvious promotion and blue shift in DRS of the heterostructure samples BC2, BC3 and BC4 was observed, implying the light absorption capacity was distinctly improved (Fig. 4a). The valence band (VB) and conduction band (CB)

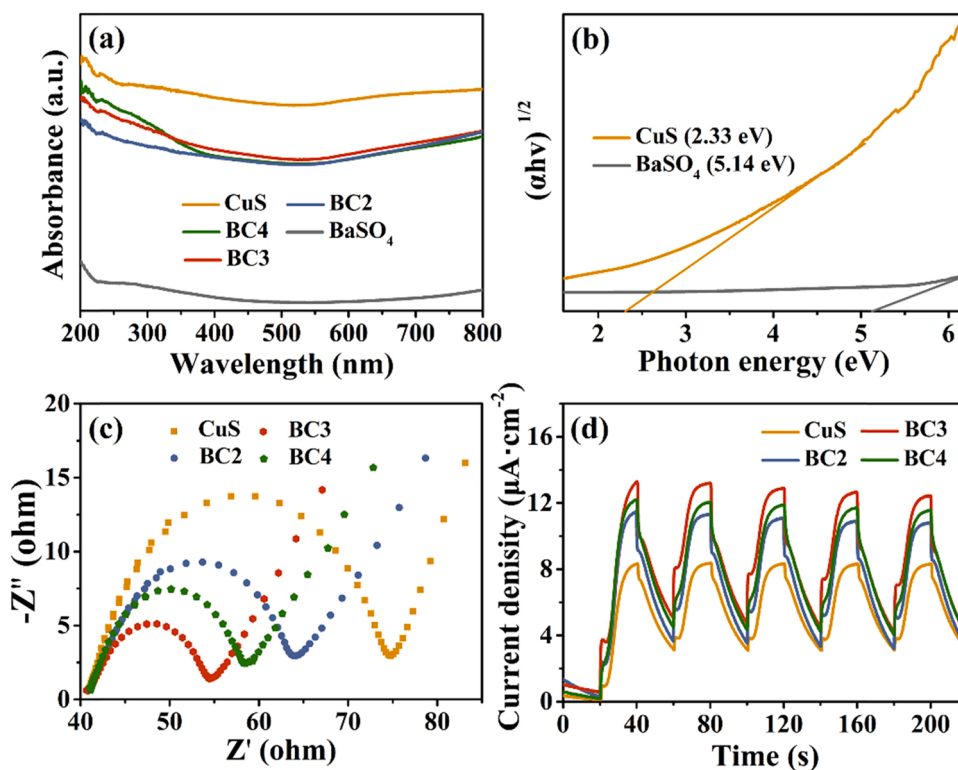


Fig. 4. UV-vis DRS of as-prepared product (a), plots of $(\alpha h\nu)^{1/2}$ versus photon energy (b), EIS Nyquist plots (c) and photocurrent responses (d) of CuS, BC2, BC3 and BC4.

potentials for CuS and BaSO₄ can be calculated based upon the following equations [47,48]:

$$E_{CB} = X - E^e - 0.5E_g$$

$$E_{VB} = E_{CB} + E_g$$

Where E_{CB} , E_{VB} , X and E^e represented CB potential, VB potential, electronegativity of catalysts and the energy of free electrons on hydrogen scale (ca. 4.5 eV), respectively. X was determined from the electronegativity of the constituent atoms and value was 6.03 and 5.33 for BaSO₄ and CuS. Hence, E_{CB} for BaSO₄ and CuS was worked out to be -1.05 and -0.34 eV and the according E_{VB} value was $+4.09$ and $+1.99$ eV, respectively.

To survey the separation and transfer process of the photogenerated electrons, series of electrochemical and fluorescence measurements were conducted. The EIS Nyquist plot of CuS possessed a large semicircle diameter, which was evidently reduced for the heterostructures (Fig. 4c). Herein, BC3 had the smallest diameter, illustrating the resistance for the photoinduced electrons transfer was markedly weakened through suitable insulator incorporation [49]. In addition, the transient photocurrent responses of the as-prepared photocatalysts were recorded under visible-light irradiation and a steady behaviour of the current density was detected, as shown in Fig. 4d. The highest photocurrent density was achieved in BC3, indicating the generation and separation of photoinduced charges were accelerated through the formation of heterostructure [50]. Similarly, the recombination of charge carriers was furthest inhibited in BC3, testified by the lowest PL spectrum in Fig. S2. Undoubtedly, the generation, separation and transfer of the photoinduced charge carriers were enormously enhanced through appropriate combination of insulator BaSO₄ and semiconductor CuS.

3.3. Adsorption and photo-degradation of tetracycline

The adsorption and photocatalytic properties of the as-synthesized catalysts were evaluated by the TC removal experiments. The dark adsorption proceeded for 30 min to reached the equilibrium and 1.3%

and 24.0% of TC was adsorbed by BaSO₄ and CuS respectively (Fig. 5a). In comparison, the BC3 heterostructure showed a three-fold improved adsorption capacity, which was mainly attributed to the intensive chemical adsorption [51,52]. As observed in the FESEM images (Fig. 2b), the pure CuS were aggregates of irregular nanoparticles, leaving insufficient adsorption active sites for TC. When taking BaSO₄ as the template, the growth model of CuS was changed and the dispersity was vastly promoted. The remark increasing of the exposed active sites of CuS played a crucial role on the strong chemisorption of TC molecules. With the increase of CuS amount in the composite, the adsorption ability of the catalyst BC4 was slightly deteriorated, which was probably resulted from the self-nucleation of CuS to form partial nanoparticle aggregates [53].

Upon the visible-light irradiation, the photocatalytic degradation stage took place and photocatalytic activity of the catalysts followed the order: BaSO₄ < CuS < Mix < BC2 < BC4 < BC3. After 120 min irradiation, totally 2.8% and 29.9% of TC was removed by BaSO₄ and CuS, respectively. Upon the formation of heterogenous structure, the TC removal efficiency was visibly elevated and the BC3 heterostructure degraded 96.8% of TC within 120 min. For comparison, the physical mixture of BaSO₄ and CuS (named Mix) was prepared and its TC removal efficiency was only 39.5%, certifying the importance of forming heterostructure. What's more, the photodegradation kinetics of the catalysts was studied. As depicted in Fig. 5b, all the degradation data were in good accordance with the pseudo-first-order kinetic model ($\ln(C_0/C) = \kappa t$), where C_0 and C represented the concentration of TC before and after photocatalytic reaction, and κ is the pseudo-first-order kinetic constant [54,55]. Noticeably, the κ of BC3 with a correlation coefficient (R^2) of 0.991 was calculated to be $1.4 \times 10^{-2} \text{ min}^{-1}$, which was 18, 21 and 311 times higher than that of Mix ($8.0 \times 10^{-4} \text{ min}^{-1}$), CuS ($6.7 \times 10^{-4} \text{ min}^{-1}$) and BaSO₄ ($4.5 \times 10^{-5} \text{ min}^{-1}$), respectively. The photocatalytic activity of BaSO₄, CuS and BC3 was further examined by ciprofloxacin (CIP) degradation, which was the third-generation quinolone antibacterial drug [56,57]. No adsorption and degradation activity were presented by BaSO₄ towards CIP. In contrast, CuS and BC3 adsorbed 29.4%

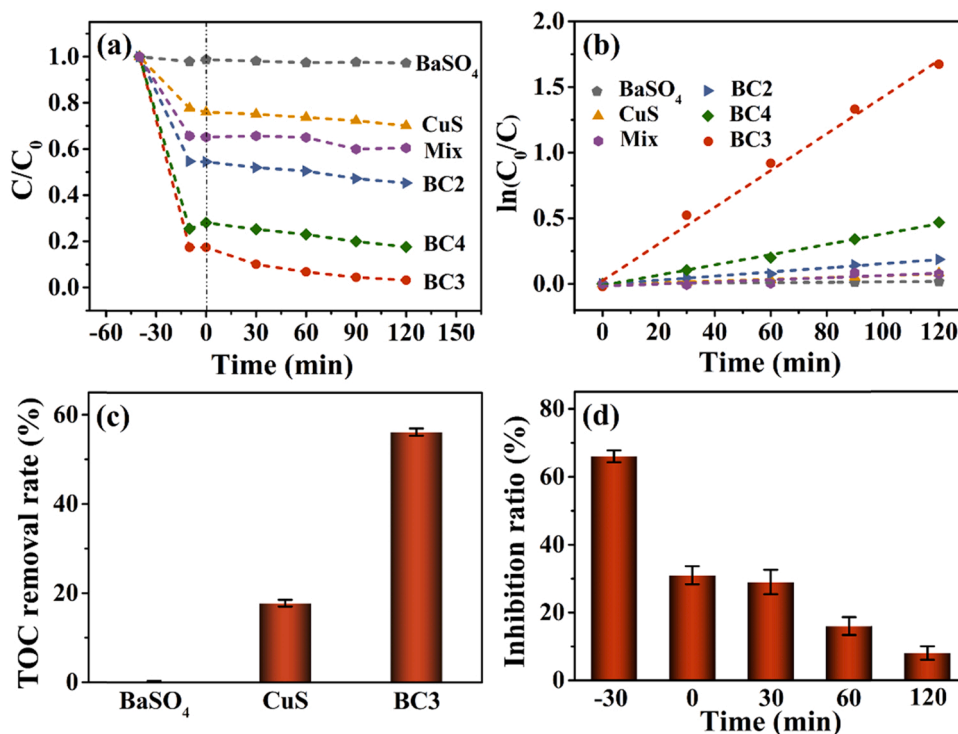


Fig. 5. TC adsorption-photodegradation processes (a) and pseudo-first-order kinetic study (b) over the as-synthesized catalysts, the removal rate of TOC over BaSO₄, CuS and BC3 (c) and inhibition ratio of *V. fischeri* during the TC removal process over BC3 (d).

and 49.7% of CIP after 30 min dark adsorption, and removed totally 37.8% and 69.1% of CIP after 2 h photo-degradation, respectively (Fig. S3a). The calculated pseudo-first-order kinetic constant of BC3 ($4.1 \times 10^{-3} \text{ min}^{-1}$) exhibited about four-fold enhancement over that of CuS ($1.1 \times 10^{-3} \text{ min}^{-1}$) (Fig. S3b). Undeniably, the construction of insulator-semiconductor heterostructure was of paramount importance for accelerating degradation rate of antibiotics.

The TOC examination was applied to evaluate the TC mineralization ability of the photocatalytic materials, where BC3 showcased a TOC removal rate about 56% (Fig. 5c). Comparably, BaSO_4 could not mineralize TC and the TOC removal rate of CuS was only 20%. The mineralization of pollutants usually resulted in the toxicity reduction and thus the variation in relative acute toxicity was monitored during the photocatalytic process over BC3 [58]. According to Fig. 5d, the *V. fischeri* inhibition ratio of the original TC solution was about 66%, which rapidly reduced to $\sim 31\%$ after 30 min dark adsorption. The bioluminescence inhibition ratio displayed little change in the first 30 min visible-light irradiation. The delay of toxicity reduction was consistent with the reported researches and could be attributed to that the degraded intermediates retaining three-ring structure possessed the similar toxicity with TC [35,59]. In the following stage, the toxicity for *V. fischeri* was gradually decreased and remained only $\sim 8\%$ at 2 h, indicating the intermediates was further degraded into less toxic products [60,61]. Although the TC molecules were not completely mineralized, the toxicity could be effectively reduced through visible-light photocatalysis by the BaSO_4 -CuS heterostructure. Moreover, we examined the activity stability of the BC3 catalysts by conducting the photocatalytic experiments for consecutive cycles (2 h per cycle). After four runs, no apparent inactivation was observed (Fig. S4), demonstrating the robust cycling performance of the BaSO_4 -CuS photocatalysts. Additionally, the XPS of the used BC3 was compared with the fresh sample. All the peak locations kept same and only negligible intensity change was showed, certifying the excellent stability and reusability of the heterostructure (Fig. S5).

Subsequently, the time-dependent full-range UV-vis spectra of CuS and BC3 were investigated to further study the TC degrading process. At 0 min, the initial TC solution showed two ultraviolet adsorption peaks at

277 and 357 nm, and 357 nm was the typical adsorption wavelength for TC. For BC3 catalyst, the absorbance of TC solution was gradually diminished with the extension of irradiation time and no visible peak displacement was noticed (Fig. 6a). The concurrent reduce of two adsorption peaks manifested that the TC molecules were decomposed into lower molecular weight organics and the produced intermediates were continuous to be degraded [62]. In contrast, the weaken of the TC adsorption peaks over CuS sample was imperceptible after 120 min irradiation (Fig. 6b). The significant difference was in good agreement with the TOC results (Fig. 5c). To survey the tremendous difference in oxidation capacity of CuS and BC3, the ESR spin-trapping with DMPO as free radical scavenger was employed to analyze the active oxidized species involved in the photodegradation process. As displayed in Fig. 6c, CuS and BC3 both produced the $\cdot\text{O}_2^-$ under visible-light irradiation. Nevertheless, the DMPO- $\cdot\text{O}_2^-$ signal of BC3 was twice stronger than that of CuS, declaring the heterostructure structure plainly benefited the activation of the small molecule O_2 [63]. Intriguingly, definite DMPO- $\cdot\text{OH}$ ESR signal was detected in BC3 in comparison with the flat ESR curve of CuS (Fig. 6d), attesting the heterostructure sample could provide stronger oxidation ability towards the TC degradation. The formation of $\cdot\text{OH}$ in BC3 perhaps went through the $\cdot\text{O}_2^-$ - H_2O_2 - $\cdot\text{OH}$ pathway and the considerable production of H_2O_2 was detected in the photocatalytic system of BC3, as exhibited in Fig. S6 [64]. No signal of DMPO- $\cdot\text{O}_2^-$ was observed in both CuS and BC3 (Fig. S7), demonstrating that $\cdot\text{O}_2^-$, H_2O_2 and $\cdot\text{OH}$ were the main active substances for TC degradation over the BaSO_4 -CuS heterostructure photocatalysts.

Importantly, the potential photodegradation pathway of TC molecules was proposed in Fig. 7 by examining the produced intermediates through LC-MS study. According to Fig. S8, the characteristic peak of the original TC molecule located at $m/z = 445$ [62], following by the successively appeared new peaks at $m/z = 461$, 417, 363, 362, 351, 340, 164 and 149. In pathway I, the production of intermediate C2 ($m/z = 417$) was attributed to the demethylation of TC and then the deamination and dihydroxylation of C2 gave rise to the intermediate C3 ($m/z = 363$). The sequent dihydroxylation resulted in the production of C4 ($m/z = 340$). It is worth noting that C4 could be attacked and oxidized by the strong active oxygen species to form small- molecule C5

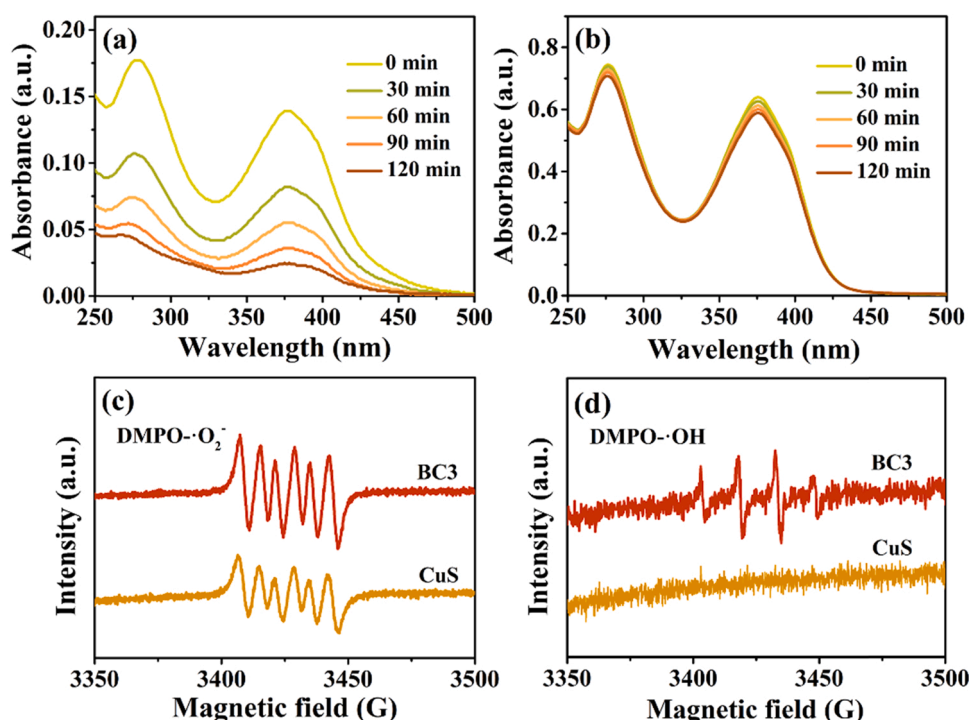


Fig. 6. Time-dependent UV-vis spectra of TC solutions over BC3 (a) and CuS (b), DMPO spin-trapping ESR spectra for $\cdot\text{O}_2^-$ (c) and $\cdot\text{OH}$ (d) over BC3 and CuS.

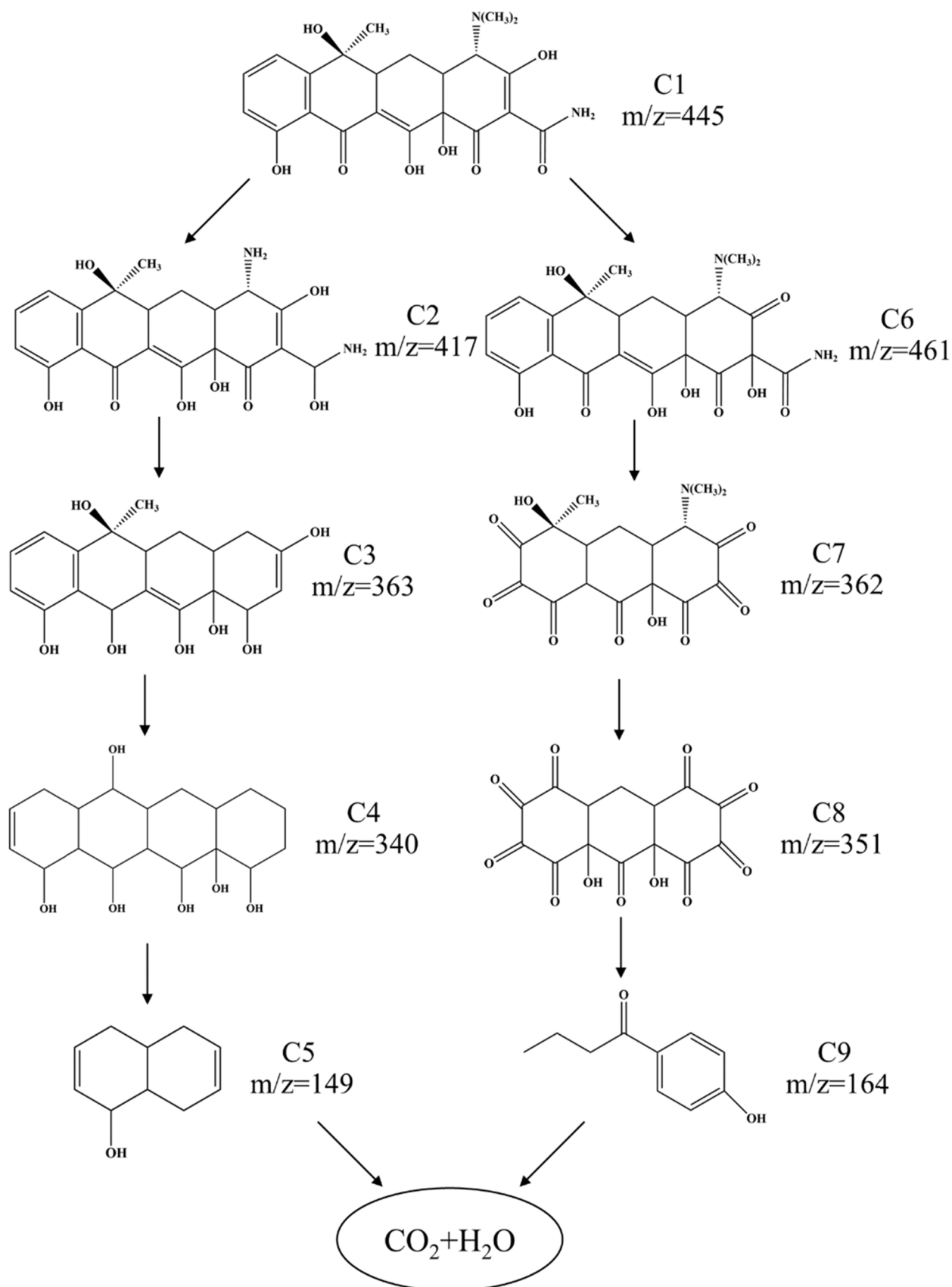


Fig. 7. Potential photodegradation pathway of TC by BC3 heterostructure.

($m/z = 149$) through cleavage of carbon-carbon bonds and the ring-opening reactions [65]. In the possible pathway II, the double bond in TC was firstly activated with the oxidizing radicals and transformed to the hydroxylation form C6 ($m/z = 461$). The double bond, amide group, $-\text{CH}_3$ and $-\text{N}(\text{CH}_3)_2$ in C6 were continuously decomposed and oxidized by the active radicals to form C7 ($m/z = 362$) and C8 ($m/z = 351$). Further ring-opening process led to the formation of C9 ($m/z = 164$) [66,67]. The small-molecule intermediate C5 and C9 could be partially fragmented into CO_2 and H_2O . The inorganic ions formed during the photocatalytic TC degradation process were also detected and quantified. After 30 min photo-degradation, the NH_4^+ were rapidly produced through the deamination of TC to reach a concentration of 0.64 mg/L, while the amount of NO_2^- and NO_3^- were relatively low (Fig. S9). As the proceeding of photocatalytic reaction, the production of NH_4^+ was slowed down, and the NH_4^+ and NO_2^- were gradually oxidized to NO_3^- . Nevertheless, concentration of NO_3^- still remained at a low level after 2 h, indicating the oxidative radicals in this system were preferentially used to degrade TC [68]. The concentration of NH_4^+ , NO_2^- and NO_3^- in the treated solution was about 0.86, 0.18 and 0.35 mg/L, respectively.

3.4. Adsorption and photo-degradation process and mechanism

Based upon the abovementioned analysis, the probable mechanism for the boosting photocatalytic activity of the insulator-semiconductor heterostructure was proposed as depicted in Fig. 8. Firstly, upon the corporation of narrow-gap CuS, the heterogenous catalysts were enabled with superior visible-light adsorption capacity [29]. The bulk BaSO_4 with high refractive index allowed the multiple reflection and scattering of the incident light, which was in favor of the sufficient light utilization by CuS to induce more photoexcited electrons. Secondly, the construction of heterogeneous structure was beneficial for elevating the photo-redox ability of the catalysts. According to DRS results, the calculated CB and VB for the p-type CuS was -0.34 and 1.99 eV with Fermi level close to VB [27,69], which was determined to be -1.05 and 4.09 eV for the n-type BaSO_4 (confirmed by the Mott-Schottky plot in Fig. S10) with Fermi level close to CB. For pure CuS, its CB potential (-0.34 eV) could narrowly meet the formation of $\cdot\text{O}_2^-$ ($\text{O}_2/\cdot\text{O}_2^- = -0.33$ eV) and could not afford the formation of $\cdot\text{OH}$ [70]. After contact

with BaSO_4 , it is legitimate that the electrons excited by CuS would transfer to the CB of BaSO_4 through the equilibrium of Fermi level [22, 28,44]. The stronger redox ability achieved by heterostructure could produce the vastly upgraded $\cdot\text{O}_2^-$ and H_2O_2 to generate $\cdot\text{OH}$. The deduction kept consistent with the ESR spin-trapping results (Fig. 6c and d).

To further verify the electron transfer in heterogeneous structure, the DFT theoretical calculations was employed to survey the interface structure of the heterostructure. Based on the HRTEM observations (Fig. 3b and c), the heterostructure interface was composed by the (210) lattice plane of BaSO_4 and the (103) plane of CuS. Accordingly, the side view of the facet contact in the BaSO_4 -CuS heterostructure was diagramed in Fig. 9a and the interface mainly consisted of the Cu and O atoms. The electron location function calculations manifested the intensive covalent interaction between Cu atoms of CuS and O atoms of BaSO_4 (Fig. 9b). The Cu-O covalent interaction tunneled the unique electronic transmission channel between the semiconductor and insulator [19]. To figure out the transfer direction of the photogenerated electrons, the charge difference distribution was calculated. As depicted in Fig. 9c, the Cu atom in CuS was charge depleted (shown in blue), while the O atom in BaSO_4 was charge accumulated (shown in yellow). This result further proved the infer that the photoexcited electrons were transferred from CuS to BaSO_4 to obtain intensified oxidative ability [21, 22]. It is worth mentioning that the effective electron transfer between CuS and BaSO_4 is also conducive to inhibit the recombination of charge carriers in CuS, which was certified by the series of electrochemical characterizations. Accordingly, the light-excited holes left in the VB of CuS were consumed for TC decomposition, further contributing to the separation of photo-induced charges and resulting in the superior chemical stability of the heterostructure photocatalysts (Fig. 5c).

What's more, the adsorption and activation of pollutants played a pivotal role on the photocatalytic reactions and thus the adsorption behavior of BaSO_4 -CuS heterostructure was thoroughly investigated. The heterostructure BC3 exhibited accomplished TC adsorption ability in nearly neutral condition at pH of 7 (87.1%) or 9 (83.9%) (Fig. S11a). However, the adsorption efficiency at pH of 3 was remarkably deteriorated to 36.3% and the possible reason was the positively charged TC in acidic medium could cause repulsion force with the catalysts [71]. As

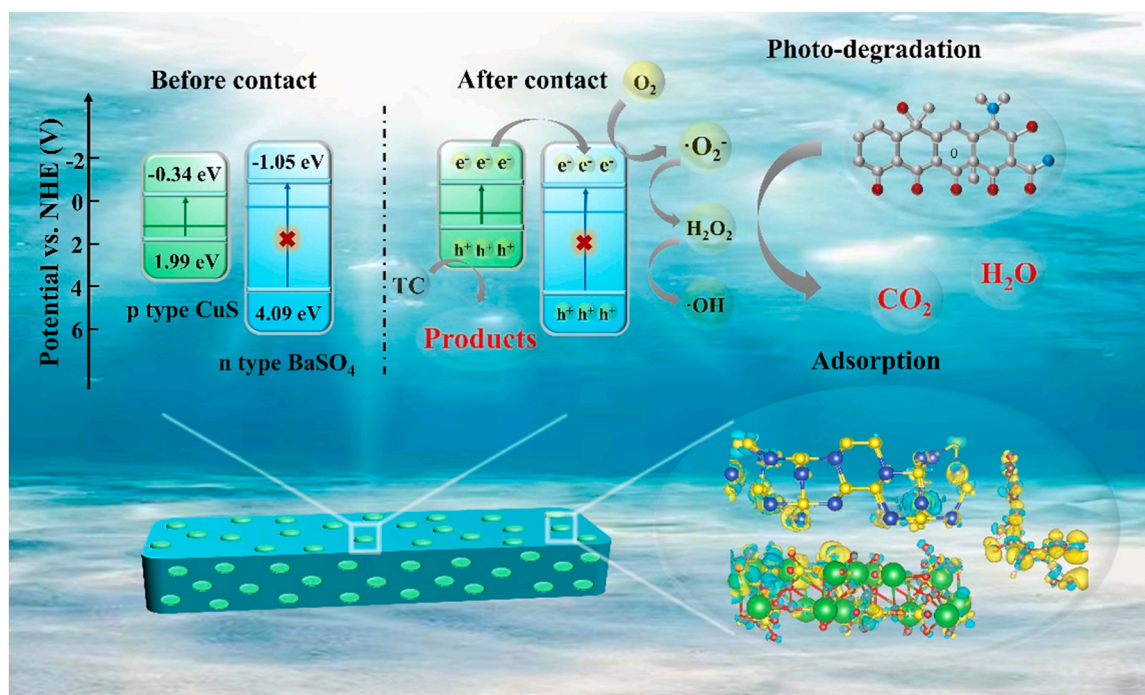


Fig. 8. Schematic illustration of the supposed mechanism for adsorption and photo-degradation of TC over BaSO_4 -CuS heterostructure.

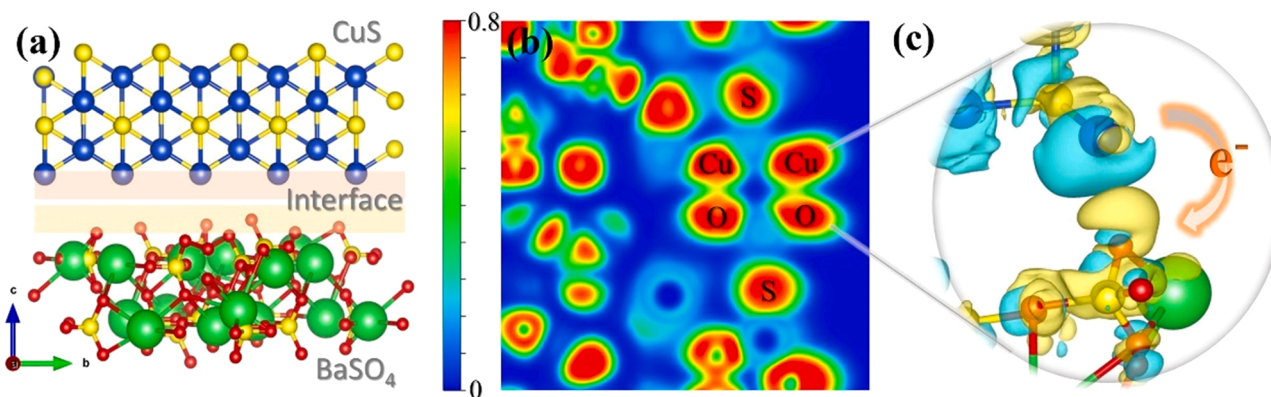


Fig. 9. Side view of the constructed BaSO₄-CuS heterostructure (a), electron location function (b) and charge difference distribution (c) of the heterostructure interface (charge accumulation is in yellow and charge depletion is in blue).

expected, the catalyst dosage showed positive correction with the TC adsorption and the adsorption amount was slightly improved from 65.6% to 82.6% when increasing catalysts from 5 mg to 20 mg (Fig. S11b). Subsequently, the adsorption kinetics were probed, utilizing pseudo-first order and pseudo-second order models to fit the experimental data (Fig. S12). It could be deduced that pseudo-second order model could better describe the adsorption process with a higher R^2 of 0.97 and the predicted q_e was 81.4 mg/g (Table S2). To gain deeper understanding of the adsorption mechanism, DFT calculations were employed to reveal the interaction between TC and the catalysts. As displayed in Fig. S13, the TC molecules adsorbed on the surface of CuS and the interface of BaSO₄-CuS heterostructure was separately observed. After contact with catalysts surface, the TC molecules were electron accumulated (shown in yellow), illustrating the electrons were transferred from photocatalysts to TC molecules to activate the pollutants. Noteworthily, the charge transfer between TC and heterostructure was much more intense than CuS, which was probably resulted from the electron-rich environment of the interface [22]. The corresponding adsorption energy of TC on CuS surface and heterostructure interface was calculated to be -0.08 and -0.62 eV, respectively. The distinctly improved TC adsorption energy of heterostructure was responsible for its superior TC adsorption capacity (Fig. 5a) and thus contributed to the enhancement of photocatalytic performance.

4. Conclusions

A strategic approach was proposed in this study for activating insulator as visible-light-driven photocatalysts. Representative insulator-semiconductor heterostructure BaSO₄-CuS was constructed via a specific core-shell structure for the highly efficient TC degradation. Combining experimental and theoretical study, the atomic and electronic structure of the heterostructure interface was elaborately investigated. The strong Cu-O covalent interaction endowed the heterogeneous structure with a unique channel to transfer photoinduced electrons from CuS to BaSO₄ to achieve strengthened redox ability for augmented generation of the active species such as $\cdot O_2^-$ and $\cdot OH$ to decompose the TC molecules. It is evidenced that the formation of heterogenous structure also contributed to the improved visible-light adsorption ability and accelerated electron separation and transfer to enhance the photocatalytic performance. The activation of BaSO₄ as photocatalysts sheds light on the development of the earth-abundant, environmental-friendly and chemically robust insulators and pave a potential path for their practical viability in environment related applications.

CCRediT authorship contribution statement

Qiaoshan Chen: Conceptualization, Methodology, Data curation,

Writing – review & editing. Hanqiang Zhou: Experiment, Investigation, Formal analysis. Jianchun Wang: Visualization, Data curation. Jinhong Bi: Supervision, Funding acquisition. Fan Dong: Supervision, Validation, Writing – review & editing, Funding acquisition.

Declaration of Competing Interest

The authors declare that they have no known competing financial interests or personal relationships that could have appeared to influence the work reported in this paper.

Acknowledgments

This work was supported by the National Natural Science Foundation of China (22176029, 51672047, 22006009), Youth Talent Support Program of Fujian Province (00387077) and the Natural Science Foundation of Fujian Province (2021J05131, 2019J01648).

Appendix A. Supporting information

Supplementary data associated with this article can be found in the online version at doi:10.1016/j.apcatb.2022.121182.

References

- [1] R. Singh, A.P. Singh, S. Kumar, B.S. Giri, K.H. Kim, Antibiotic resistance in major rivers in the world: a systematic review on occurrence, emergence, and management strategies, *J. Clean. Prod.* 234 (2019) 1484–1505.
- [2] Y. Ben, C. Fu, M. Hu, L. Liu, M.H. Wong, C. Zheng, Human health risk assessment of antibiotic resistance associated with antibiotic residues in the environment: a review, *Environ. Res.* 169 (2019) 483–493.
- [3] E. Yeşilova, B. Osman, A. Kara, E. Tümay Özer, Molecularly imprinted particle embedded composite cryogel for selective tetracycline adsorption, *Sep. Purif. Technol.* 200 (2018) 155–163.
- [4] Z. He, X. Wang, Y. Luo, Y. Zhu, X. Lai, J. Shang, J. Chen, Q. Liao, Effects of suspended particulate matter from natural lakes in conjunction with coagulation to tetracycline removal from water, *Chemosphere* 277 (2021), 130327.
- [5] T. Lu, X. Xu, X. Liu, T. Sun, Super hydrophilic PVDF based composite membrane for efficient separation of tetracycline, *Chem. Eng. J.* 308 (2017) 151–159.
- [6] R. Guan, X. Yuan, Z. Wu, L. Jiang, J. Zhang, Y. Li, G. Zeng, D. Mo, Efficient degradation of tetracycline by heterogeneous cobalt oxide/cerium oxide composites mediated with persulfate, *Sep. Purif. Technol.* 212 (2019) 223–232.
- [7] S. Shao, X. Wu, Microbial degradation of tetracycline in the aquatic environment: a review, *Crit. Rev. Biotechnol.* 40 (2020) 1010–1018.
- [8] H. Wang, L. Zhang, Z. Chen, J. Hu, S. Li, Z. Wang, J. Liu, X. Wang, Semiconductor heterojunction photocatalysts: design, construction, and photocatalytic performances, *Chem. Soc. Rev.* 43 (2014) 5234–5244.
- [9] T.S. Natarajan, K.R. Thampi, R.J. Tayade, Visible light driven redox-mediator-free dual semiconductor photocatalytic systems for pollutant degradation and the ambiguity in applying Z-scheme concept, *Appl. Catal. B-Environ.* 227 (2018) 296–311.
- [10] L. Rimoldi, D. Meroni, G. Cappelletti, S. Ardizzone, Green and low cost tetracycline degradation processes by nanometric and immobilized TiO₂ systems, *Catal. Today* 281 (2017) 38–44.

- [11] T. Lu, Y. Gao, Y. Yang, H. Ming, Z. Huang, G. Liu, D. Zheng, J. Zhang, Y. Hou, Efficient degradation of tetracycline hydrochloride by photocatalytic ozonation over Bi₂WO₆, *Chemosphere* 283 (2021), 131256.
- [12] Y. Wang, H. Liu, B. Wu, T. Zhou, J. Wang, J. Zhou, S. Li, F. Cao, G. Qin, Preparation and visible-light-driven photocatalytic property of AgX (X = Cl, Br, I) nanomaterials, *J. Alloy. Compd.* 776 (2019) 948–953.
- [13] J. Yu, J. Kiwi, I. Zivkovic, H.M. Rønnow, T. Wang, S. Rtimi, Quantification of the local magnetized nanotube domains accelerating the photocatalytic removal of the emerging pollutant tetracycline, *Appl. Catal. B-Environ.* 248 (2019) 450–458.
- [14] Y. Pi, X. Li, Q. Xia, J. Wu, Y. Li, J. Xiao, Z. Li, Adsorptive and photocatalytic removal of Persistent Organic Pollutants (POPs) in water by metal-organic frameworks (MOFs), *Chem. Eng. J.* 337 (2018) 351–371.
- [15] F. Dong, T. Xiong, Y.J. Sun, L.L. Lu, Y.X. Zhang, H.J. Zhang, H.W. Huang, Y. Zhou, Z.B. Wu, Exploring the photocatalysis mechanism on insulators, *Appl. Catal. B-Environ.* 219 (2017) 450–458.
- [16] W. Cui, L.C. Chen, J.Y. Li, Y. Zhou, Y.J. Sun, G.M. Jiang, S.C. Lee, F. Dong, Vacancy induces semiconductor-like photocatalysis on insulator BaSO₄, *Appl. Catal. B-Environ.* 253 (2019) 293–299.
- [17] K. Li, S. Zhang, Q. Tan, X. Wu, Y. Li, Q. Li, J. Fan, K. Lv, Insulator in photocatalysis: essential roles and activation strategies, *Chem. Eng. J.* 426 (2021), 130772.
- [18] S. Jin, G. Dong, J. Luo, F. Ma, C. Wang, Improved photocatalytic NO removal activity of SrTiO₃ by using SrCO₃ as a new co-catalyst, *Appl. Catal. B-Environ.* 227 (2018) 24–34.
- [19] H. Wang, Y.J. Sun, W.J. He, Y. Zhou, S.C. Lee, F. Dong, Visible light induced electron transfer from a semiconductor to an insulator enables efficient photocatalytic activity on insulator-based heterojunctions, *Nanoscale* 10 (2018) 15513–15520.
- [20] J. Liu, C. Zhang, B. Ma, T. Yang, X. Gu, X. Wang, J. Zhang, C. Hu, Rational design of photoelectron-trapped/accumulated site and transportation path for superior photocatalyst, *Nano Energy* 38 (2017) 271–280.
- [21] H. Wang, Y.J. Sun, G.M. Jiang, Y.X. Zhang, H.W. Huang, Z.B. Wu, S.C. Lee, F. Dong, Unraveling the mechanisms of visible light photocatalytic NO purification on earth-abundant insulator-based core-shell heterojunctions, *Environ. Sci. Technol.* 52 (2018) 1479–1487.
- [22] H. Wang, W. Cui, X.A. Dong, J.Y. Li, Q.S. Chen, Z.M. Wang, Y.J. Sun, J.P. Sheng, Y. Zhou, Y.X. Zhang, F. Dong, Interfacial activation of reactants and intermediates on CaSO₄ insulator-based heterostructure for efficient photocatalytic NO removal, *Chem. Eng. J.* 390 (2020) 8.
- [23] J. Low, J. Yu, M. Jaroniec, S. Wageh, Ahmed A. Al-Ghamdi, Heterojunction photocatalysts, *Adv. Mater.* 29 (2017), 1601694.
- [24] C.W. Siao, H.L. Chen, L.W. Chen, J.L. Chang, T.W. Yeh, C.C. Chen, Controlled hydrothermal synthesis of bismuth oxychloride/bismuth oxybromide/bismuth oxyiodide composites exhibiting visible-light photocatalytic degradation of 2-hydroxybenzoic acid and crystal violet, *J. Colloid Interface Sci.* 526 (2018) 322–336.
- [25] J. Low, J. Yu, M. Jaroniec, S. Wageh, A.A. Al-Ghamdi, Heterojunction photocatalysts, *Adv. Mater.* 29 (2017), 1601694.
- [26] J. Xue, J. Liu, Y. Liu, H. Li, Y. Wang, D. Sun, W. Wang, L. Huang, J. Tang, Recent advances in synthetic methods and applications of Ag₂S-based heterostructure photocatalysts, *J. Mater. Chem. C* 7 (2019) 3988–4003.
- [27] D. Majhi, Y.P. Bhoi, P.K. Samal, B.G. Mishra, Morphology controlled synthesis and photocatalytic study of novel CuS-Bi₂O₃ heterojunction system for chlorpyrifos degradation under visible light illumination, *Appl. Surf. Sci.* 455 (2018) 891–902.
- [28] Z. Wu, X. Liu, C. Yu, F. Li, W. Zhou, L. Wei, Construct interesting CuS/TiO₂ architectures for effective removal of Cr(VI) in simulated wastewater via the strong synergistic adsorption and photocatalytic process, *Sci. Total Environ.* 796 (2021), 148941.
- [29] D. Hong, W. Zang, X. Guo, Y. Fu, H. He, J. Sun, L. Xing, B. Liu, X. Xue, High piezophotocatalytic efficiency of CuS/ZnO nanowires using both solar and mechanical energy for degrading organic dye, *ACS Appl. Mater. Interfaces* 8 (2016) 21302–21314.
- [30] Y. Hong, J. Zhang, F. Huang, J. Zhang, X. Wang, Z. Wu, Z. Lin, J. Yu, Enhanced visible light photocatalytic hydrogen production activity of CuS/ZnS nanoflower spheres, *J. Mater. Chem. A* 3 (2015) 13913–13919.
- [31] X. Zhang, X. He, Z. Kang, M. Cui, D.-P. Yang, R. Luque, Waste eggshell-derived dual-functional CuO/ZnO/eggshell nanocomposites: (photo)catalytic reduction and bacterial inactivation, *ACS Sustain. Chem. Eng.* 7 (2019) 15762–15771.
- [32] S. Álvarez-Torrellas, A. Rodríguez, G. Ovejero, J. García, Comparative adsorption performance of ibuprofen and tetracycline from aqueous solution by carbonaceous materials, *Chem. Eng. J.* 283 (2016) 936–947.
- [33] Y. Ni, J. Yang, L. Sun, Q. Liu, Z. Fei, X. Chen, Z. Zhang, J. Tang, M. Cui, X. Qiao, La/LaF₃ co-modified MIL-53(Cr) as an efficient adsorbent for the removal of tetracycline, *J. Hazard. Mater.* 426 (2022), 128112.
- [34] C.H. Han, H.D. Park, S.B. Kim, V. Yargeau, J.W. Choi, S.H. Lee, J.A. Park, Oxidation of tetracycline and oxytetracycline for the photo-Fenton process: Their transformation products and toxicity assessment, *Water Res.* 172 (2020), 115514.
- [35] M.H. Khan, H. Bae, J.Y. Jung, Tetracycline degradation by ozonation in the aqueous phase: proposed degradation intermediates and pathway, *J. Hazard. Mater.* 181 (2010) 659–665.
- [36] X. Qiao, F. Zhang, F. Sha, J. Zhao, H. Shi, J. Zhang, Controllable synthesis of nanostructured BaSO₄ and BaSO₃ crystals on the basis of DMSO oxidation chemistry, *CrystEngComm* 20 (2018) 173–180.
- [37] A. Khan, U. Alam, W. Raza, D. Bahemann, M. Muneer, One-pot, self-assembled hydrothermal synthesis of 3D flower-like CuS/g-C₃N₄ composite with enhanced photocatalytic activity under visible-light irradiation, *J. Phys. Chem. Solids* 115 (2018) 59–68.
- [38] K. Das, D. Majhi, Y.P. Bhoi, B.G. Mishra, Combustion synthesis, characterization and photocatalytic application of CuS/Bi₂TiO₅ p-n heterojunction materials towards efficient degradation of 2-methyl-4-chlorophenoxyacetic acid herbicide under visible light, *Chem. Eng. J.* 362 (2019) 588–599.
- [39] Y. Wan, S. Du, C. Lu, K. Ren, B. Shi, S. Liu, C. Li, W. Dou, P. Fang, N. Ye, Metallic CuS decorated CdS nanowires for efficient photocatalytic H₂ evolution under visible-light irradiation, *J. Alloy. Compd.* 871 (2021), 159461.
- [40] S. Zhang, X. Mou, Z. Cui, C. Hou, W. Yang, H. Gao, X. Luo, Partial sulfidation for constructing Cu₂O-CuS heterostructures realizing enhanced electrochemical glucose sensing, *New J. Chem.* 45 (2021) 7204–7209.
- [41] R. Yang, H. Li, Y. Wang, Z. Zhu, C. Hu, T. Zhao, W. Wang, B. Liu, A novel flower-like Z-type heterojunction CuS/Bi₂O₃ composite catalyst prepared under mild conditions for degradation of antibiotics and sterilization under visible light, *Environ. Sci. Nano* 7 (2020) 3074–3087.
- [42] X. Dai, L. Chen, Z. Li, X. Li, J. Wang, X. Hu, L. Zhao, Y. Jia, S.X. Sun, Y. Wu, Y. He, CuS/KTa_{0.75}Nb_{0.25}O₃ nanocomposite utilizing solar and mechanical energy for catalytic N₂ fixation, *J. Colloid Interface Sci.* 603 (2021) 220–232.
- [43] J. Liu, S. Zou, B. Lou, C. Chen, L. Xiao, J. Fan, Interfacial electronic interaction induced engineering of ZnO-BiOI heterostructures for efficient visible-light photocatalysis, *Inorg. Chem.* 58 (2019) 8525–8532.
- [44] L. Zhang, C. Hu, H. Ji, p-AgI anchored on {001} facets of n-Bi₂O₂CO₃ sheets with enhanced photocatalytic activity and stability, *Appl. Catal. B-Environ.* 205 (2017) 34–41.
- [45] Q. Li, X. Du, C. Xia, X. Wang, T. Yang, Y. Jiang, Z. Yang, D. Zhu, F. Yin, Fabrication and photocatalytic properties of nano CuS/MoS₂ composite catalyst by dealloying amorphous Ti-Cu-Mo alloy, *Appl. Surf. Sci.* 467–468 (2019) 221–228.
- [46] P.J. Mafa, B.B. Mamba, A.T. Kuvarega, Construction of hierarchical BiPw₁₂O₄₀/BiOI p-n heterojunction with enhanced visible light activity for degradation of endocrine disrupting Bisphenol A, *Sep. Purif. Technol.* 253 (2020), 117349.
- [47] F. Chen, Q. Yang, J. Sun, F. Yao, S. Wang, Y. Wang, X. Wang, X. Li, C. Niu, D. Wang, G. Zeng, Enhanced photocatalytic degradation of tetracycline by AgI/BiVO₄ heterojunction under visible-light irradiation: mineralization efficiency and mechanism, *ACS Appl. Mater. Interfaces* 8 (2016) 32887–32900.
- [48] S. Li, S. Hu, W. Jiang, Y. Liu, J. Liu, Z. Wang, Facile synthesis of flower-like Ag₃VO₄/Bi₂WO₆ heterojunction with enhanced visible-light photocatalytic activity, *J. Colloid Interface Sci.* 501 (2017) 156–163.
- [49] L. Paramanik, K.H. Reddy, K.M. Parida, Stupendous photocatalytic activity of p-BiOI/n-PbTiO₃ heterojunction: the significant role of oxygen vacancies and interface coupling, *J. Phys. Chem. C* 123 (2019) 21593–21606.
- [50] X. Liu, R. Guo, H. Qin, Z. Wang, X. Shi, W. Pan, J. Tang, P. Jia, Y. Miao, J. Gu, Fabrication of Bi₂O₃(OH)NO₃/g-C₃N₄ nanocomposites for efficient CO₂ photocatalytic reduction, *Colloid Surf. A* 580 (2019), 123782.
- [51] T. Wu, Q. Xue, F. Liu, J. Zhang, C. Zhou, J. Cao, H. Chen, Mechanistic insight into interactions between tetracycline and two iron oxide minerals with different crystal structures, *Chem. Eng. J.* 366 (2019) 577–586.
- [52] Q. Li, M. Ji, X. Li, H. Song, G. Wang, C. Qi, A. Li, Efficient co-removal of copper and tetracycline from aqueous solution by using permanent magnetic cation exchange resin, *Bioresour. Technol.* 293 (2019), 122068.
- [53] X. Bai, Y.J. Wang, Y. Li, X.J. Wang, Adsorption-photocatalytic remediation for series of tetracycline contaminants with BiOCl-CdS composite under simulated sunlight, *J. Taiwan Inst. Chem. Eng.* 104 (2019) 94–105.
- [54] Z. Wei, D. Benlin, Z. Fengxia, T. Xinyue, X. Jiming, Z. Lili, L. Shiyin, D.Y.C. Leung, C. Sun, A novel 3D plasmonic p-n heterojunction photocatalyst: Ag nanoparticles on flower-like p-Ag₂S/n-BiVO₄ and its excellent photocatalytic reduction and oxidation activities, *Appl. Catal. B-Environ.* 229 (2018) 171–180.
- [55] Y. Fu, M. Zhang, P. Wang, Y. Zhang, C. Xu, Q. Yan, Constructing a Z-scheme 3D hollow pineal-like AgBr/Bi₂O₃ hybrid material based on ameliorated p-n heterostructure towards exorbitant photocatalytic performance, *J. Alloy. Compd.* 861 (2021), 157944.
- [56] X.J. Wen, C.G. Niu, L. Zhang, C. Liang, H. Guo, G.M. Zeng, Photocatalytic degradation of ciprofloxacin by a novel Z-scheme CeO₂-Ag/AgBr photocatalyst: influencing factors, possible degradation pathways, and mechanism insight, *J. Catal.* 358 (2018) 141–154.
- [57] B. Wang, J. Di, P. Zhang, J. Xia, S. Dai, H. Li, Ionic liquid-induced strategy for porous perovskite-like PbBiO₂Br photocatalysts with enhanced photocatalytic activity and mechanism insight, *Appl. Catal. B-Environ.* 206 (2017) 127–135.
- [58] L. Qin, Z. Wang, Y. Fu, C. Lai, X. Liu, B. Li, S. Liu, H. Yi, L. Li, M. Zhang, Z. Li, W. Cao, Q. Niu, Gold nanoparticles-modified MnFe₂O₄ with synergistic catalysis for photo-Fenton degradation of tetracycline under neutral pH, *J. Hazard. Mater.* 414 (2021), 125448.
- [59] X.D. Zhu, Y.J. Wang, R.J. Sun, D.M. Zhou, Photocatalytic degradation of tetracycline in aqueous solution by nanosized TiO₂, *Chemosphere* 92 (2013) 925–932.
- [60] J. Li, L. Zhao, R. Zhang, H.H. Teng, L.P. Padhye, P. Sun, Transformation of tetracycline antibiotics with goethite: mechanism, kinetic modeling and toxicity evaluation, *Water Res.* 199 (2021), 117196.
- [61] M.C. Dodd, H.P.E. Kohler, U. Von, Gunten, Oxidation of antibacterial compounds by ozone and hydroxyl radical: elimination of biological activity during aqueous ozonation processes, *Environ. Sci. Technol.* 43 (2009) 2498–2504.
- [62] Q. Wang, H. Zhu, B. Li, Synergy of Ti-O-based heterojunction and hierarchical 1D nanobelt/3D microflower heterostructures for enhanced photocatalytic tetracycline degradation and photoelectrochemical water splitting, *Chem. Eng. J.* 378 (2019), 122072.
- [63] J. Li, C. Xiao, K. Wang, Y. Li, G. Zhang, Enhanced generation of reactive oxygen species under visible light irradiation by adjusting the exposed facet of FeWO₄

- nanosheets to activate oxalic acid for organic pollutant removal and Cr(VI) reduction, *Environ. Sci. Technol.* 53 (2019) 11023–11030.
- [64] W. Wang, P. Xu, M. Chen, G. Zeng, C. Zhang, C. Zhou, Y. Yang, D. Huang, C. Lai, M. Cheng, L. Hu, W. Xiong, H. Guo, M. Zhou, Alkali metal-assisted synthesis of graphite carbon nitride with tunable band-gap for enhanced visible-light-driven photocatalytic performance, *ACS Sustain. Chem. Eng.* 6 (2018) 15503–15516.
- [65] Z. Li, X. Wang, N. Xu, Y. Xiao, L. Ma, J. Duan, Cost-effective and visible-light-driven melamine-derived sponge for tetracyclines degradation and *Salmonella* inactivation in water, *Chem. Eng. J.* 394 (2020), 124913.
- [66] Y. Lin, X. Wu, Y. Han, C. Yang, Y. Ma, C. Du, Q. Teng, H. Liu, Y. Zhong, Spatial separation of photogenerated carriers and enhanced photocatalytic performance on Ag_3PO_4 catalysts via coupling with PPy and MWCNTs, *Appl. Catal. B-Environ.* 258 (2019), 117969.
- [67] Y. Pan, X. Yuan, L. Jiang, H. Wang, H. Yu, J. Zhang, Stable self-assembly $\text{AgI}/\text{UiO}-66(\text{NH}_2)$ heterojunction as efficient visible-light responsive photocatalyst for tetracycline degradation and mechanism insight, *Chem. Eng. J.* 384 (2020), 123310.
- [68] L. Ge, Y. Yue, W. Wang, F. Tan, S. Zhang, X. Wang, X. Qiao, P.K. Wong, Efficient degradation of tetracycline in wide pH range using MgNCN/MgO nanocomposites as novel H_2O_2 activator, *Water Res.* 198 (2021), 117149.
- [69] C. Lai, M. Zhang, B. Li, D. Huang, G. Zeng, L. Qin, X. Liu, H. Yi, M. Cheng, L. Li, Z. Chen, L. Chen, Fabrication of CuS/BiVO_4 (0 4 0) binary heterojunction photocatalysts with enhanced photocatalytic activity for Ciprofloxacin degradation and mechanism insight, *Chem. Eng. J.* 358 (2019) 891–902.
- [70] J. Wang, G. Zhang, J. Li, K. Wang, Novel three-dimensional flowerlike $\text{BiOBr}/\text{Bi}_2\text{SiO}_5$ p–n heterostructured nanocomposite for degradation of tetracycline: enhanced visible light photocatalytic activity and mechanism, *ACS Sustain. Chem. Eng.* 6 (2018) 14221–14229.
- [71] N. Amaly, A.Y. El-Moghazy, N. Nitin, G. Sun, P.K. Pandey, Synergistic adsorption-photocatalytic degradation of tetracycline by microcrystalline cellulose composite aerogel doped with montmorillonite hosted methylene blue, *Chem. Eng. J.* 430 (2022), 133077.